The Journal of Immunology

RESEARCH ARTICLE | MARCH 06 2023

NF-κB–Inducing Kinase Governs the Mitochondrial Respiratory Capacity, Differentiation, and Inflammatory Status of Innate Immune Cells

Justin N. Keeney; ... et. al

J Immunol (2023) 210 (8): 1123–1133.
https://doi.org/10.4049/jimmunol.2200596

NF-κB–Inducing Kinase Governs the Mitochondrial Respiratory Capacity, Differentiation, and Inflammatory Status of Innate Immune Cells

Justin N. Keeney,* Ashley D. Winters,† Raquel Sitcheran,* and A. Phillip West†

NF-κB–inducing kinase (NIK), which is essential for the activation of the noncanonical NF-κB pathway, regulates diverse processes in immunity, development, and disease. Although recent studies have elucidated important functions of NIK in adaptive immune cells and cancer cell metabolism, the role of NIK in metabolic-driven inflammatory responses in innate immune cells remains unclear. In this study, we demonstrate that murine NIK-deficient bone marrow–derived macrophages exhibit defects in mitochondrial-dependent metabolism and oxidative phosphorylation, which impair the acquisition of a prorepair, anti-inflammatory phenotype. Subsequently, NIK-deficient mice exhibit skewing of myeloid cells characterized by aberrant eosinophil, monocyte, and macrophage cell populations in the blood, bone marrow, and adipose tissue. Furthermore, NIK-deficient blood monocytes display hyperresponsiveness to bacterial LPS and elevated TNF-α production ex vivo. These findings suggest that NIK governs metabolic rewiring, which is critical for balancing proinflammatory and anti-inflammatory myeloid immune cell function. Overall, our work highlights a previously unrecognized role for NIK as a molecular rheostat that fine-tunes immunometabolism in innate immunity, and suggests that metabolic dysfunction may be an important driver of inflammatory diseases caused by aberrant NIK expression or activity. ***The Journal of Immunology*****, 2023, 210: 1123–1133.**

Macrophages are important components of the innate immune system that play key roles in immunity, tissue homeostasis, and cancer (1). Macrophages exist across a spectrum of polarization states in vivo and can adopt proinflammatory or anti-inflammatory properties depending on local cytokine gradients and tissue residency (2). Murine bone marrow–derived macrophages (BMDMs) can be polarized toward the extreme end of the proinflammatory spectrum by culture in bacterial LPS or IFN-γ. These so-called M1 or M(LPS) macrophages produce proinflammatory cytokines such as TNF-α, have bactericidal and phagocytic functionality, and can produce reactive oxygen species (ROS) and NO (3). Conversely, BMDMs cultured in IL-4 are skewed toward the anti-inflammatory end of the spectrum. These so-called M2 or M(IL-4) macrophages can dampen inflammatory responses by secreting anti-inflammatory cytokines such as IL-10, promote extracellular matrix remodeling, and enhance stromal cell proliferation (3). It is well appreciated that metabolic switches promote the acquisition of distinct macrophage polarization states and play pivotal roles in the final effector cell functionality (4). M1 macrophages upregulate glycolysis, have a broken tricarboxylic acid (TCA) cycle, and display impaired oxidative phosphorylation (OXPHOS), leading to enhanced generation of TCA intermediates such as succinate and other metabolites necessary for ROS and NO generation (5–7). In contrast, M2 macrophages have an intact TCA cycle and upregulate OXPHOS and fatty acid oxidation to generate anti-inflammatory products such as glucocorticoids, IL-10, IL-13, etc. (8, 9). These metabolic shifts are critical for macrophage function, because small molecules that inhibit the major metabolic enzymes in glycolysis, TCA, and OXPHOS can dramatically alter polarization states in vitro and in vivo (10–12).

NF-κB signaling has a well-established role in inflammatory processes with the canonical NF-κB pathway rapidly responding to inflammatory stimuli (13). Alternatively, the noncanonical NF-κB pathway, which requires NF-κB–inducing kinase (NIK; also known as MAP3K14), regulates immune cell differentiation, development, and tissue homeostasis (13–16). Over the last decade, NIK has been found to play many novel roles in a diverse set of immune cells and their progenitors (17, 18). Within the bone marrow, NIK promotes mitochondrial biogenesis during osteoclastogenesis (14). In microglia, which are tissue-resident macrophages of the brain, NIK is important for the induction of cytokine expression, which aids in T cell recruitment in an animal model of experimental autoimmune encephalomyelitis (19, 20).

*Department of Cell Biology and Genetics, School of Medicine, Texas A&M University, Bryan, TX; and †Department of Microbial Pathogenesis and Immunology, School of Medicine, Texas A&M University, Bryan, TX

ORCIDs: 0000-0003-1748-0971 (J.N.K.); 0000-0001-8916-9707 (R.S.); 0000-0003-2884-6895 (A.P.W.).

Received for publication August 12, 2022. Accepted for publication February 12, 2023.

This work was supported by the National Heart, Lung, and Blood Institute, National Institutes of Health (Grant R01HL148153 to A.P.W.) and the National Institute of Neurological Disorders and Stroke, National Institutes of Health (R01NS082554 to R.S.). Additional support was provided by a voucher from the Texas A&M Center for Environmental Health Research (TiCER) NIEHS P30 ESES029067, a pilot award from the Texas A&M School of Medicine and an X-Grant from the Texas A&M University Office of the Vice President for Research.

The data presented in this article have been submitted to the Gene Expression Omnibus (https://www.ncbi.nlm.nih.gov/geo/query/acc.cgi?acc=GSE223040) under accession number GSE223040.

Address correspondence and reprint requests to Dr. Raquel Sitcheran or Dr. A. Phillip West, Department of Cell Biology and Genetics, Texas A&M University School of Medicine, 8447 Riverside Parkway, 1359 TAMU, Bryan, TX 77807 (R.S.) or Department of Microbial Pathogenesis and Immunology, School of Medicine, Texas A&M University, MREB I, 3012, Bryan, TX (A.P.W.). E-mail addresses: sitcheran@tamu.edu (R.S.) or awest@tamu.edu (A.P.W.)

The online version of this article contains supplemental material.

Abbreviations used in this article: BMDM, bone marrow–derived macrophage; FMLP, *N*-formyl-Met-Leu-Phe; gRNA, guide RNA; IKK, inhibitor of nuclear factor κ-B kinase; MD, mitochondrial disease; mROS, mitochondrial reactive oxygen species; NIK, NF-κB–inducing kinase; NIK^{KO}, NF-κB–inducing kinase knockout; NIK^{WT}, wild-type NF-κB–inducing kinase; OCR, oxygen consumption rate; OXPHOS, oxidative phosphorylation; PID, primary immunodeficiency disease; ROS, reactive oxygen species; SRC, spare respiratory capacity; TCA, tricarboxylic acid; WAT, white adipose tissue.

Recently, we and others have demonstrated roles for NIK in regulating mitochondrial function and metabolism in cancer cells (19, 21–23). For example, we previously reported that NIK regulates mitochondrial dynamics (21) and promotes oxidative metabolism (22) in glioblastoma, an aggressive form of brain cancer. Moreover, NIK-deficient glioblastoma cells exhibit impaired mitochondrial fission and increased glycolysis to compensate for diminished oxidative metabolism (21, 22) and are less invasive. These novel metabolic roles of NIK are largely independent of noncanonical NF-κB signaling, suggesting that NIK plays a direct role in regulating mitochondrial function. Another recent study showed that NIK shapes the metabolism of CD8 T cells independently of noncanonical NF-κB by stabilizing hexokinase 2 and promoting NADPH generation (23). Similar metabolic changes were observed in B cells containing a deletion of TNFR-associated factor 3, an upstream inhibitor of NIK (24). Although NIK has emerged as a key regulator of tumor cell and lymphocyte metabolism, whether NIK regulates immunometabolic switches in myeloid innate immune cells remains unclear.

Studies using NIK knockout (NIK^{KO}) mice have revealed that NIK deficiency promotes a dramatic increase in peripheral blood eosinophil abundance (25). NIK^{KO} mice develop a hypereosinophilic inflammatory disease driven by the infiltration of pathogenic eosinophilic granulocytes into diverse organs, including skin, liver, lung, and esophagus, leading to early death (25, 26). Recent studies have shown that eosinophils upregulate OXPHOS on activation (27); however, it remains unclear whether immunometabolic switches contribute to the inflammatory myeloid phenotypes observed in NIK^{KO} mice. To begin to address this knowledge gap, we measured mitochondrial and metabolic parameters in BMDMs from NIK^{KO} mice. In this article, we show that NIK promotes oxidative metabolism in macrophages, and that loss of NIK results in hyperinflammatory myeloid skewing of the bone marrow, blood, and other tissues. Our findings demonstrate that NIK is an important molecular rheostat that maintains mitochondrial function to control innate immune cell function, and they suggest that metabolic alterations may contribute to diseases where NIK activity is dysregulated.

Materials and Methods

Mice

All animal experiments were performed in accordance with animal use protocols with approved Institutional Animal Care and Use Committee guidelines at Texas A&M University. *Map3k14* null mice were purchased from The Jackson Laboratory (strain 025557) and maintained by heterozygous breeding. *Map3k14* floxed mice were obtained from Genentech and bred with LysMCre mice (Jackson Lab strain 004781). Equivalent numbers of male and female mice were used for all experiments. Animal numbers used are described in the figure legends.

Reagents

A comprehensive list of Abs, reagents, and primers is provided in Tables I, II, and III, respectively.

Flow cytometry

Blood and spleen immune phenotyping. Whole mouse blood was collected in sodium heparin tubes. Spleens were collected and filtered through a 100-μM cell strainer. RBCs were lysed twice with ACK lysis buffer, and leukocytes were subjected to LPS stimulation (1 μg/ml) in the presence of brefeldin A and monensin for 4 h. Fc receptors were blocked with anti-mouse CD16/CD32 (2.4G2) Ab, and cells were stained with Abs against surface proteins, permeabilized with Foxp3/Transcription Factor Staining Buffer Kit (TNB-0607-KIT; Tonbo Biosciences), and stained with Abs against intracellular proteins. Cells were analyzed with a Cytek Aurora 5L Spectral Analyzer. The results were plotted and analyzed using FlowJo software (BD Biosciences).

Bone marrow phenotyping. Cells were isolated from the tibia and femurs of mice as described later (see later *Cell culture* section). After an ACK lysis step, 500,000 cells/mouse were taken for immune cell phenotyping, and 1 million cells were stained for the stem cell analysis. Cells were stained in a 96-well plate with Live/Dead Fix Violet (eBioscience) at 4°C for 20 min. After being washed thoroughly, cells were blocked with FC blocker (eBioscience) for 10 min at 4°C before the addition of the primary Ab mixture, which incubated with the cells for 30 min. After, cells were washed and fixed with 4% paraformaldehyde for 10 min at room temperature in the dark. Flow cytometric analysis was performed on a BD Fortessa X-20 (BD Biosciences). The results were plotted and analyzed using FlowJo software (BD Biosciences).

Fat and small intestine immune phenotyping. Visceral fat deposits and a 5-cm section of the ileum were harvested from mice and washed with PBS before being placed in a 0.2% (2 mg/ml) collagenase 2 solution (Worthington Biochemical), diluted in RIPA Lysis and Extraction Buffer (Life Technologies, ThermoFisher Scientific), under constant stirring for 60 min at 37°C. The isolated cells were filtered through a 70-μM cell strainer, and RBCs were lysed with ACK lysis buffer (VWR). Cells were then stained as described earlier for the bone marrow.

Mitochondrial flow cytometry assays. This assay was previously described (28), but in brief, wild-type NIK (NIK^{WT}) and NIK^{KO} BMDMs were treated with 20 ng/ml IL-4 for 5 h before cells were detached using PBS containing 1 mM EDTA (Life Technologies, ThermoFisher Scientific). Cells were then stained with a combination of MitoTracker Green FM, MitoTracker Red FM, MitoSOX, Anti-MO CD11b, and Violet Live/Dead dye for 15 min in a 37°C tissue culture incubator. Cells were then washed twice before analysis on a BD Fortessa X-20 flow cytometer. The results were plotted and analyzed using FlowJo software (BD Biosciences).

Cell culture

L929 and HEK293T cells were obtained from the American Type Culture Collection and maintained in DMEM (Life Technologies, ThermoFisher Scientific) supplemented with 10% FBS (VWR). BMDMs were generated by crushing the tibia and femurs of unpooled mice. After lysis of RBCs with ACK lysis buffer (VWR), cells were filtered through a 40-μM cell strainer and grown on petri plates in DMEM containing 10% FBS and 30% L929 conditioned media for 7 d, with fresh L929-containing media being added on day 4 postplating. IL-4 (PeproTech) was used at a concentration of 20 ng/ml for in vitro experiments unless otherwise stated. Human U937 monocytic cells were a gift from Dr. K. Patrick and maintained in RPMI 1640 Medium (Life Technologies, ThermoFisher Scientific) supplemented with 10% FBS. To differentiate U937 monocytes into macrophages, we treated cells with 100 ng/ml PMA (AmBeed) for 48 h. After that time period the media were changed, and cells were treated similarly as BMDMs. All cells were cultured at 37°C with 95% humidity and 5% CO_2.

Lentiviral production

Twenty-four micrograms of each Lenti-CrispR-V2 plasmid containing a guide RNA (gRNA) against NIK and 72 μg of polyethyleneimine were used to transfect HEK293T cells. After 3 d of transfection, viral supernatant was harvested and filtered through a 0.45-μM syringe filter. After filtration, viral particles were concentrated 20-fold to 400 μl using Lenti-X Concentrator (631231; Clontech), and 100 μl of concentrated virus was used to infect cells. A total of 1 μg/ml puromycin (InvivoGen) was used for selection until no nontransduced cells were alive.

CRISPR-Cas9 gene knockout

U937 cells were transduced with a mixture of Lenti-CrispR-v2 viruses carrying three gRNAs for each target. The gRNA sequences for human NIK were previously described (20, 21). Loss of NIK was confirmed by immunoblot of puromycin-resistant cells. Single-colony cells were isolated by serial dilution. All experiments were repeated with at least three knockdown clones.

Immunoblotting

The protein was collected from cells lysed in RIPA buffer (Life Technologies) supplemented with protease and phosphatase inhibitors (Thermo Scientific). Lysate was then sonicated for 5 min on ice (Bioruptor UCD-200, Diagenode) before spinning down insoluble proteins for 5 min at 5000 × RPM at 4 °C. The protein was quantified using a Bradford assay reagent (BioRad) and stored at −80 °C. After running equal amounts of protein on an SDS-PAGE gel, protein was transferred onto a 0.45 μm polyvinylidene fluoride membrane (EMD Millipore) through an overnight transfer at 4 °C. After transfer, the membrane was stained with Ponceau S and the gel with GelCode blue with both being imaged on a BioRad ChemiDoc MP Imaging System. The Ponceau S was briefly washed off with Tris-buffered saline with Tween-20 before blocking the membrane in 4% BSA-PBS solution for 1 hour at room temperature. After blocking, the membranes were incubated in primary Abs (see Table I) at 4 °C overnight in blocking buffer. The following day, after washing, membranes were incubated with HRP-conjugated secondary Abs at room temperature for 1 h before developing with the

Immobilon Western Chemilum HRP Substrate (EMD Millipore) and imaging on the BioRad ChemiDoc MP Imaging System.

Seahorse extracellular flux analysis

The Seahorse XFe96 Analyzer (Agilent) was used to measure mitochondrial respiration. A total of 5×10^4 cells were plated per well in at least triplicate in 100 μl of DMEM containing 10% FBS in an Agilent Seahorse XF96 Cell Culture Microplate. After allowing the cells to settle at room temperature for 1 h, cells were moved to a 37°C incubator for 3 h until stimulated overnight with 20 ng/ml IL-4. After 16 h, the cells were washed and replaced with XF assay medium (Base Medium Minimal DMEM supplemented with 200 mM L-glutamine [pH 7.4]) and incubated with a 37°C incubator without CO2 for an hour before analysis. The oxygen consumption rate (OCR) was measured after sequential addition of 25 mM glucose, 1.5 μM oligomycin A (Sigma-Aldrich), 1.5 μM Carbonyl cyanide-*p*-trifluoromethoxyphenylhydrazone FCCP (Sigma-Aldrich) plus 1 mM sodium pyruvate (Life Technologies, ThermoFisher Scientific), and 2.5 μM antimycin A (Sigma-Aldrich) plus 1.25 μM rotenone (Enzo Life Sciences) following a previously published protocol (29).

NIK inhibition. The same workflow described above was used with the exception of incubating cells with DMSO or 5 μM B022 (MedChem Express) for up to 5 h before treating the cells overnight with 20 ng/ml IL-4.

RNA sequencing

A total of 1×10^6 NIK^{WT} and NIK^{KO} BMDMs were stimulated with 20 ng/ml IL-4 or PBS for 6 h before being lifted with PBS containing 1 mM EDTA (Life Technologies, ThermoFisher Scientific). Cells were spun down and washed once with PBS before being flash frozen in liquid nitrogen. Cell pellets were shipped on dry ice to Genewiz, where they isolated the RNA, constructed the sequencing library, and conducted the sequencing. RNA sequencing data were analyzed using the Salmon pipeline (version 1.4.0-gompi-2020b) on the Texas A&M High Performance Research Computing Cluster. Salmon was used to align the results to the reference genome *Mus musculus* GRCm39. The data were then processed through DESeq2 (version 1.32.0) on R Studio, where the annotated gene expression files were used to determine statistically significant changes in gene expression in stimulated NIK^{KO} BMDMs relative to stimulated NIK^{WT} BMDMs. Ingenuity Pathway Analysis software (QIAGEN) was used to identify gene families and potential upstream regulators within the datasets. GraphPad Prism was used to make heatmaps. The data discussed in this publication have been deposited in NCBI's Gene Expression Omnibus and are accessible through Gene Expression Omnibus Series accession number GSE223040 (https://www.ncbi.nlm.nih.gov/geo/query/acc.cgi?acc=GSE223040).

Gene expression

A total of 5×10^5 NIK^{WT} and NIK^{KO} BMDMs were stimulated with 20 ng/ml IL-4 for 6 h before being lifted with PBS containing 1 mM EDTA (Life Technologies, ThermoFisher Scientific). Cells were spun down and washed once with PBS before total RNA was isolated from cells by Purelink RNA Mini Kit (Life Technologies). cDNA was synthesized from 1 μg total RNA using iScript reverse transcription supermix (Bio-Rad) following the manufacturer's protocol. Quantitative RT-PCR was performed using Universal SYBR Green Supermix with StepOnePlus Real-Time PCR System (Applied Biosystems). Data were graphed as a $2^{\Delta\Delta CT}$ fold change with the gene expression data being normalized to the housekeeping gene *Rps18*.

Table I. Primary Abs and Ab-based reagents used in the study

Catalog Number	Company	Reagent	Conjugate
Stem cell panel			
A15423	Invitrogen	Anti-MO CD117/c-Kit	Allophycocyanin-Cy7
15-5981-81	Invitrogen	Anti-MO Ly-6A/E (SCA1)	PE-Cy5
25-0481-80	Invitrogen	Anti-MO CD48	PE-Cy7
12-1351-81	Invitrogen	Anti-MO CD135	PE
17-1502-80	Invitrogen	Anti-MO CD150	Allophycocyanin
11-0341-82	Invitrogen	Anti-MO CD34	FITC
Immune panel			
25-0032-80	Invitrogen	Anti-MO CD3	PE-Cy7
12-0452-81	Invitrogen	Anti-MO CD45R (B220)	PE
11-5931-81	Invitrogen	Anti-MO Ly-6G	FITC
35-0451-80	Invitrogen	Anti-MO CD45	PE-Cy5.5
17-0112-81	Invitrogen	Anti-MO CD11b	Allophycocyanin
155505	BioLegend	Anti-MO Siglec F	PE
In vivo polarization			
117351	BioLegend	Anti-MO CD11c	Allophycocyanin
144509	BioLegend	Anti-MO CD193 (CCR3)	FITC
123111	BioLegend	Anti-MO F4/80	PE-Cy5
Blood and spleen immune phenotyping			
25-0112-U100	Tonbo Biosciences	Anti-HU/MO M1/70 (CD11b)	Allophycocyanin-Cy7
115539	BioLegend	Anti-MO CD19	BV605
100267	BioLegend	Anti-MO CD3	Allophycocyanin-Fire810
65-4801-U100	Tonbo Biosciences	Anti-MO F4/80	PerCP-Cy5.5
128049	BioLegend	Anti-MO Ly6C	BV650
50-1276-U100	Tonbo Biosciences	Anti-MO Ly-6G	PE
107643	BioLegend	Anti-MO MHCII	BV711
506324	BioLegend	Anti-MO TNF-α	PE-Cy7
13-0871-T100	Tonbo Biosciences	Viability	Ghost Dye 710
70-0161-U100	Tonbo Biosciences	Anti-MO CD16/CD32 (Fc Shield) (2.4G2)	
ELISA kit			
41-9234-P002	Tonbo Biosciences	Mouse IL-10 ELISA Matched Ab Pair Kit	
Immunofluorescence			
MABT166	Millipore	Anti-TFAM	
CBL186	Millipore	Anti-DNA	
N-20	Santa Cruz Biotechnology	Anti-HSP60	
Western blotting			
4994	Cell Signaling	Anti-NIK	
2697	Cell Signaling	Anti-pIKKα/IKKβ S176/180	
OP133	EMD Millipore	Anti-IKKα	
4882	Cell Signaling	Anti-p100/p52	
SC-365062	Santa Cruz Biotechnology	Anti-GAPDH	
SC-69879	Santa Cruz Biotechnology	Anti–β-Actin	
SC-5274	Santa Cruz Biotechnology	Anti–β-Tubulin	
4661T	Cell Signaling	Anti-VDAC1	

Immunofluorescence

BMDMs were grown on 12-mm coverslips at 6×10^5 cells/well. Cells were treated with 200 ng/ml LPS for 24 h. After washing in PBS, cells were fixed with 4% paraformaldehyde for 20 min, permeabilized with 0.1% Triton X-100 in PBS for 5 min, blocked with PBS containing 5% FBS for 30 min, stained with primary Abs for 1 h, and stained with secondary Abs for 1 h. Cells were washed with PBS containing 5% FBS between each step. Coverslips were mounted with Prolong Gold anti-fade reagent containing DAPI (Molecular Probes). Cells were imaged on an Olympus FV3000 confocal laser scanning microscope using a 100× oil-immersed objective.

Mitochondrial isolation

A total of 2×10^6 NIK^{WT} and NIK^{KO} BMDMs were plated in a six-well plate and treated as described previously (22). At the time of harvest, cells were washed with PBS and scraped into a 1.5-ml tube before spinning down. PBS was replaced with 0.5 ml isolation buffer (320 mM sucrose, 1 mM EDTA, 10 mM HEPES [pH 7.2] with KOH and stored at 4°C) containing protease inhibitors (ThermoFisher Scientific). While on ice, cells in isolation buffer were passed through a 27-gauge needle 10 times before spinning at $700 \times g$ for 8 min at 4°C. Supernatant was removed and placed into a new tube and kept on ice while the pellet was resuspended in 0.5 mL isolation buffer with protease inhibitors before spinning at $700 \times g$ for 5 min at 4°C. Supernatant was removed and added with the previous supernatant, pellet contains the nucleus, and the 1 ml of supernatant was spun down at $17{,}000 \times g$ for 11 min at 4°C. After spinning, the supernatant was placed into a new tube labeled cytoplasm, and the pellet was resuspended in isolation buffer and spun down at $17{,}000 \times g$ for 11 min at 4°C. After this last spin, the supernatant was discarded, the mitochondrial pellet was resuspended in 40 μl isolation buffer, and the protein concentration was measured using a bicinchoninic acid assay kit (ThermoFisher Scientific) and the Victor X3 microplane reader (Perkin Elmer).

Electron transport chain activity assays

Electron transport chain activity assays were obtained from Cayman Chemical Company and manufacturer's directions were followed with the following changes. A total of 50 μl of tube A was added to each well in the 96-well plate, but activity buffer was used in place of the supplied mitochondria. We then added 5 μg of mitochondrial protein (isolation described earlier) to a total volume of 20 μl activity buffer per well. 30 μl of tube B was next added to start the reaction. Reactions were conducted at 25°C using an Epoch microplate reader with readings taken every 45 s for 20 min.

ELISA

A total of 2×10^6 NIK^{WT} or NIK^{KO} BMDMs were plated in a six-well plate and allowed to adhere overnight. The following day, the cells were treated with PBS or 20 ng/ml IL-4 for 24 h. Media were then removed from the cells, spun down, and frozen at −20°C until ready for analysis (cells were used for other experiments). IL-10 ELISA-matched Abs were obtained from Tonbo Biosciences, and the ELISA was carried out according to the manufacturer's instructions. TMB substrate was used to detect the peroxidase-labeled secondary Ab in the ELSIA kit (KPL). A total of 100 μl of undiluted media was used and run in duplicate for each biological replicate.

Macrophage haptotaxis assay

This assay was described previously (30). In brief, NIK^{WT} and NIK^{KO} BMDMs were stimulated with IL-4 (20 ng/ml) for 24 h before being lifted with PBS containing 1 mM EDTA (Life Technologies, ThermoFisher Scientific). A total of 75,000 DiO-labeled (ThermoFisher Scientific) BMDMs were plated on the insert of an 8.0-μm pore polyester membrane Transwell Permeable Support (Corning Incorporated), which was precoated for 3 h at 37°C with 4 μg/ml fibrinogen (Sigma-Aldrich). After letting the cells settle for 3 h, the media were removed and a Matrigel Matrix (50% Matrigel, 49% culture media, 1% FBS) was added on top of the cell layer (Corning Incorporated). Once the Matrigel matrix solidified, a solution of 100 nM *N*-formyl-Met-Leu-Phe (FMLP; Sigma-Aldrich) was added to the top of the Matrigel to induce a chemokine gradient. Cells were allowed to migrate for 24 h before z-stack images were acquired on a Nikon A1R Confocal microscope (Nikon Instruments). Images were then processed in Imaris 9.5.0 (Oxford Instruments) before counting the number of cells invaded. Data were graphed as a fold change to NIK^{WT} of the number of total cells that invaded.

Macrophage adhesion assay

This assay was described previously (30). In brief, NIK^{WT} and NIK^{KO} BMDMs were stimulated with IL-4 (20 ng/ml) for 24 h before being lifted with PBS containing 1 mM EDTA (Life Technologies, ThermoFisher

Table II. Commercial reagents used in the study

Catalog Number	Supplier	Reagent
L31963	Invitrogen	Violet Live/Dead dye
14-9161-71	Invitrogen	HU FCR binding inhibitor
M36008	Invitrogen	MitoSOX
M22425	Invitrogen	MitoTracker Red FM
M7514	Invitrogen	MitoTracker Green FM
8778s	Cell Signaling	MitoTracker Deep Red FM
TLRL-PB5LPS	Invivogen	Ultrapure LPS-B5
214-14	PeproTech	Recombinant murine IL-4
LS004174	Worthington Biochemical	Collagenase, type 2
LS004186	Worthington Biochemical	Collagenase, type 4
354234	Corning	Matrigel basement membrane matrix
F3879	Sigma-Aldrich	Fibrinogen
341584	Sigma-Aldrich	Polyvinyl alcohol
C35007	Invitrogen	CyQUANT
D275	Invitrogen	DiO
F3506	Sigma-Aldrich	FMLP
TNB-0607-KIT	Tonbo Biosciences	Foxp3/Transcription Factor Staining Buffer Kit
75351	Sigma-Aldrich	Oligomycin A
15218	Cayman Chemical	FCCP
A8674	Sigma-Aldrich	Antimycin A
ALX-350-360-G001	Enzo Life Sciences	Rotenone
1708891	BioRad	iScript
A25742	Universal SYBR Green	Invitrogen
700930	Cayman Chemical	MitoCheck Complex I Activity Assay Kit
700940	Cayman Chemical	MitoCheck Complex II Activity Assay Kit
700950	Cayman Chemical	MitoCheck Complex II/III Activity Assay Kit
700990	Cayman Chemical	MitoCheck Complex IV Activity Assay Kit
701000	Cayman Chemical	MitoCheck Complex V Activity Assay Kit
5120-0075	KPL	TMB substrate
15702-10	Polysciences Inc.	1-μm carboxylate microspheres/FITC
HY-120501	MedChem Express	B022 NIK inhibitor
P7170-1	Sigma-Aldrich	Ponceau S
24592	Thermo Scientific	GelCode Blue

Table III. Oligonucleotides used in quantitative real-time PCR

Gene name	Refseq ID	Forward primer	Reverse primer
Cd163	NM_053094.2	5'–CATCCGCCTTTGAATCCATCTCTTG–3'	5'–CCTCCTCATTGTCTTCCTCCTGTG–3'
Arg1	NM_007482.3	5'–ACCTGGCCTTTGATGTCCCTA–3'	5'–AGAGATGCTTCCAACTGCCAGACT–3'
Rps18	NM_011296.3	5'–ACTTTTGGGGCCTTCGTGTC–3'	5'–GCCCAGAGACTCATTTCTTCTTG–3'

Scientific). Cells were diluted to a concentration of 1 million cells/ml, and 50 μl of cell solution was plated on a precoated 4 μg/ml fibrinogen and 0.5% polyvinyl alcohol (Sigma-Aldrich) 96-well plate. Cells were plated with technical replicates and allowed to sit for 30 min in a 37°C tissue culture incubator. Cells were then washed once with PBS before staining the adhered cells with the CyQUANT DNA stain according to the manufacturer's instructions (Invitrogen, ThermoFisher Scientific). Fluorescence signal was measured on the Victor X3 microplate reader, and cell number was determined through a standard curve of cells.

Macrophage phagocytosis assay

NIK^{WT} and NIK^{KO} BMDMs were plated subconfluently in a six-well plate before being stimulated with IL-4 (20 ng/ml) for 24 h. A total of 10^8 1-μm carboxylate microspheres (Polysciences) were coated in a 50% mouse serum (MP Biomedicals) solution and incubated for 30 min at 37°C. The solution was then diluted to 5% serum before being added to cells and allowed to incubate for 2 h. After, cells were washed twice with PBS before fixing with 4% PFA. Once the PFA was washed, cells were stained with Phalloidin and Hoechst (Invitrogen, ThermoFisher Scientific) and imaged on a Nikon Eclipse Ti microscope.

Statistical analysis

Statistical analyses were carried out using GraphPad Prism, and details can be found in the figure legends where applicable. The data presented in this article were considered statistically significant at $p < 0.05$.

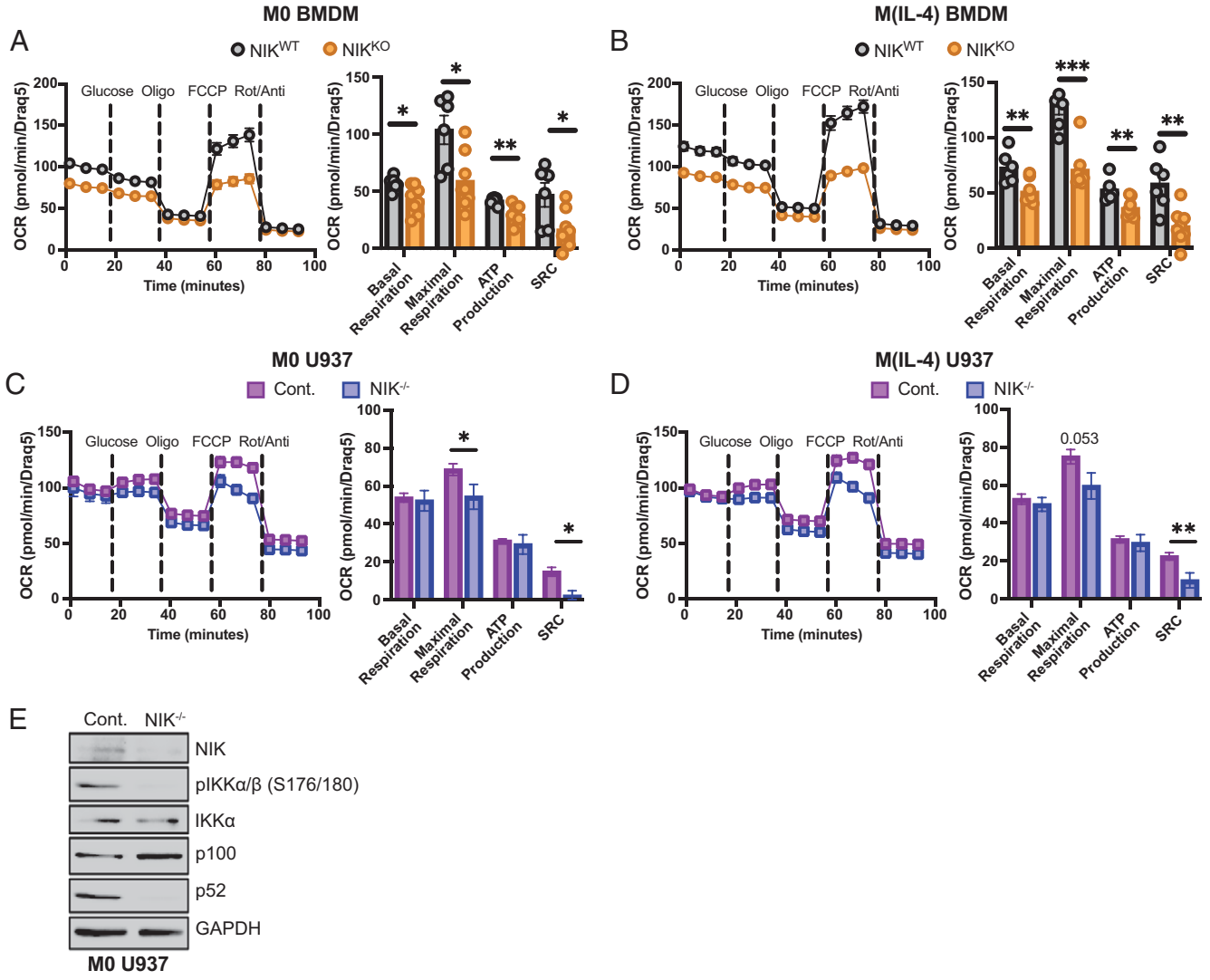

FIGURE 1. NIK regulates oxidative metabolism in macrophages. Seahorse extracellular flux analysis investigating changes in the OCR of basal (M0) NIK^{WT} and NIK^{KO} BMDMs (**A**) or after an overnight treatment with IL-4 [M(IL-4)] (**B**). Line graphs are combined technical ($n > 23$) and biological replicates, with bar graphs representing the averaged technical replicate value for each animal ($n > 6$ biological replicates). Data are mean ± SEM, and statistics are a Student *t* test; $*p < 0.05$, $**p < 0.01$, $***p < 0.001$. Seahorse extracellular flux analysis showing (**C**) OCR readouts of basal (M0) and (**D**) IL-4–treated [M(IL-4)] control and $NIK^{-/-}$ U937 cells. Graphs represent three independent experiments with treatment conditions run in at least technical triplicates (n = three single-cell isolated clones). Data are mean ± SEM, and statistics are a Student *t* test; $*p < 0.05$, $**p < 0.01$. (**E**) Representative Western blot verifying loss of NIK in U937 cells using the empty CRISPR vector, LCV2, as a control. Samples were treated with 200 ng/ml LPS and 10 μM MG132 for 4 h before extracting protein with RIPA Lysis and Extraction Buffer.

Results

NIK regulates macrophage metabolism by shaping mitochondrial respiratory capacity and OXPHOS complex activity

To investigate how NIK regulates innate immune cell function, we examined metabolic shifts during the polarization of BMDMs obtained from NIK^{WT} and NIK^{KO} mice. After differentiation in L929-conditioned media for 7 d, we noted that M0 macrophages from NIK^{KO} mice displayed reduced basal and maximal respiration, as well as impaired mitochondrial spare respiratory capacity (SRC) (Fig. 1A). On treatment with IL-4 to stimulate an M2-like phenotype [M(IL-4)], NIK^{KO} BMDMs were unable to increase basal and maximal respiration, abrogating SRC and indicating a pronounced and persistent defect in oxidative metabolism (Fig. 1B). Decreased maximal respiration and SRC were also observed in M0 and M(IL-4) NIK CRISPR knockout ($NIK^{-/-}$) human monocytic U937 cells after their differentiation into macrophages (Fig. 1C–E and Table I). Similar decreases in basal and maximal respiration were observed in NIK conditional knockout BMDMs (LysMCre; $NIK^{fl/fl}$) and in NIK^{WT} BMDMs treated with the NIK inhibitor B022 (31) (Supplemental Fig. 1). Taken together, these data indicated that NIK regulates oxidative metabolism by controlling OXPHOS and maximal respiration.

To gain insight into the underlying OXPHOS deficit in NIK^{KO} BMDMs, we performed RNA sequencing on M0 and M(IL-4) skewed BMDMs. We did not observe significant changes in the expression of genes involved in glycolysis, TCA cycle, pentose phosphate pathway, glucose transporters, or electron transport chain subunits (Supplemental Fig. 2), indicating that loss of respiratory capacity in NIK^{KO} BMDMs occurs at a posttranscriptional level. However, we did note a significant increase in mitochondrial superoxide production in both M0 and M(IL-4) NIK^{KO} BMDMs compared with NIK^{WT} (Fig. 2A, 2B and Table II), indicating enhanced electron leak from inefficient respiratory complexes. Mitochondrial ROS (mROS) can be produced from OXPHOS complexes I, II, and III, so we next performed enzymatic assays with isolated mitochondria to assess respiratory complex efficiency. Consistent with our mROS data, we observed that NIK^{KO} BMDMs exhibited impaired activity of complexes I and II compared with NIK^{WT} BMDMs (Fig. 2C, 2D). This apparent electron transport chain defect correlated with defects in other markers of mitochondrial fitness, including increased numbers of mitochondria in the NIK^{KO} BMDMs with reduced membrane potential (Supplemental Fig. 3A–C) and a trend toward increased mitochondrial size (Supplemental Fig. 3E–G). Complexes III–V exhibited no changes in activity between NIK^{WT} and NIK^{KO}, regardless of treatment with IL-4 (Fig. 2E–G). Similar to our previous findings in cancer cells (21, 22), NIK localized to the mitochondria after treatment with IL-4 (Supplemental Fig. 3D). These data suggest that mitochondria-associated NIK controls oxidative metabolism and electron transport chain function through OXPHOS complexes I and II.

NIK^{KO} macrophages fail to polarize to an M(IL-4) phenotype in vitro and in vivo

Further analysis of macrophage gene signatures revealed significant defects in M2-related wound healing genes in the NIK^{KO} BMDMs compared with NIK^{WT} in response to IL-4 treatment (Fig. 3A). The RNA sequencing data were verified via quantitative RT-PCR for changes in expression of typical IL-4 response genes (Table III), such as arginase 1 (*Arg1*) and *CD163*, and a significant decrease in expression was observed in *Arg1* in the NIK^{KO} BMDMs compared with NIK^{WT} (Fig. 3B). Consistent with this finding, we observed a significant decrease in IL-10 secretion to the cell culture media in response to IL-4 treatment (Fig. 3C). In addition, after IL-4 treatment, we observed that NIK^{KO} BMDMs harbored functional defects in migration and adhesion (Fig. 3D, 3E), although their phagocytic capabilities remained intact (Fig. 3F). Taken together with the metabolic findings discussed earlier, these data suggest that NIK^{KO} BMDMs fail to fully polarize into an M(IL-4) phenotype because of a deficiency in OXPHOS activity.

Eosinophils have been shown to secrete IL-4 and promote an M(IL-4) macrophage phenotype in vivo (32–35). Increased peripheral and tissue eosinophil numbers have been previously described in NIK^{KO} mice and are associated with dermatitis and esophageal eosinophilia (25, 26). Because little is known about the role of NIK in macrophages, we investigated the relationship between the accumulated

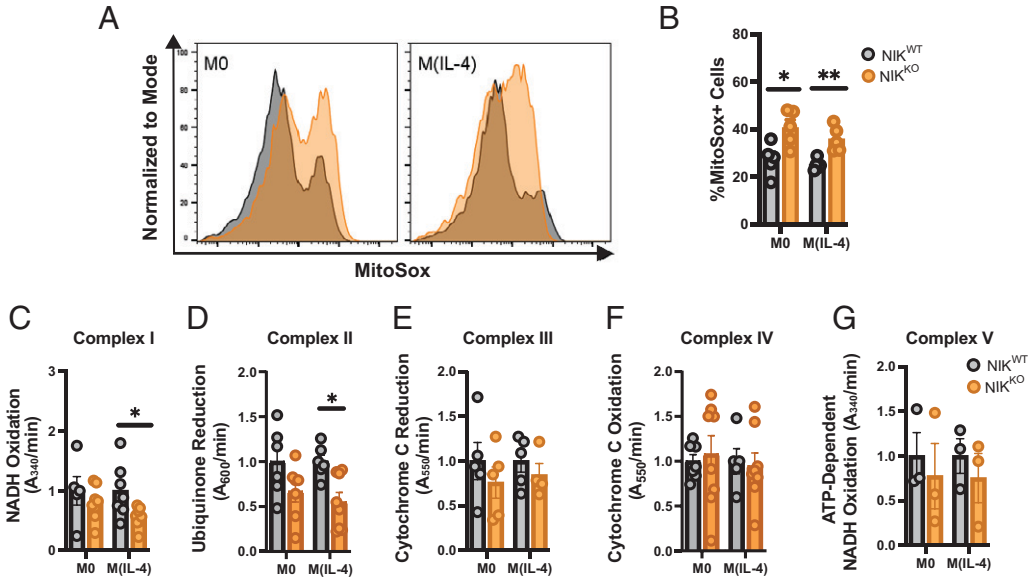

FIGURE 2. NIK-deficient macrophages display elevated mROS and impaired OXPHOS complex I and II activity. (**A** and **B**) Representative histograms and quantification of MitoSOX levels in NIK^{WT} and NIK^{KO} BMDMs after 6-h treatment with IL-4 ($n = 5$ biological replicates). Statistics are a Student *t* test; $*p < 0.05$, $**p < 0.01$. Electron transport chain activity assays for complex I (**C**), complex II (**D**), complex III (**E**), complex IV (**F**), and complex V (**G**) using isolated mitochondria from basal or 24-h IL-4–treated NIK^{WT} and NIK^{KO} BMDMs. Graphs represent biological replicates ($n > 3$ biological replicates run in at least duplicate). Statistics are a Student *t* test; $*p < 0.05$.

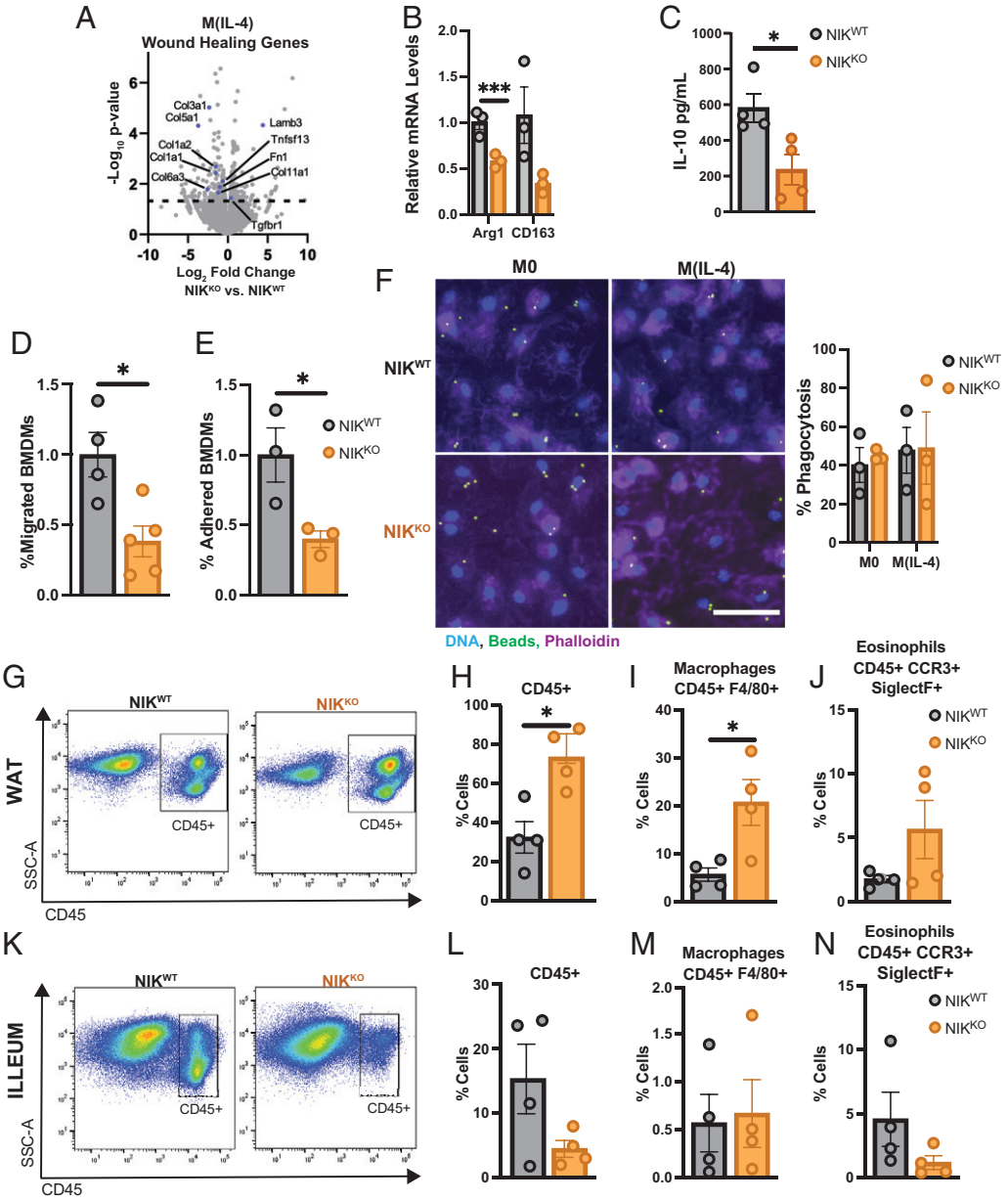

FIGURE 3. NIK^{KO} macrophages fail to polarize to an M(IL-4) phenotype in vitro and in vivo. (**A**) RNA sequencing data of classical prorepair pathways in NIK^{KO} macrophages after 6 h of IL-4 treatment. Volcano plots represent two biological replicates with a log2fold change of NIK^{KO} BMDMs compared with NIK^{WT} of the same treatment. Statistics were calculated by DESeq2, and genes above the dotted line are deemed significant for having a $-\log(p \text{ value}) > 1.3$. (**B** and **C**) The trends in RNA sequencing were confirmed by assessing IL-4 response genes by quantitative RT-PCR (B) and validating IL-10 levels by ELISA after 24-h IL-4 treatment in NIK^{WT} and NIK^{KO} macrophages (C) ($n > 3$ biological replicates run in triplicates). Statistics are a Student t test; $^*p < 0.05$, $^{***}p < 0.001$. NIK^{WT} and NIK^{KO} BMDMs were stimulated for 24 h with IL-4 before undergoing the following assays: (**D**) cell invasion assay was performed with media containing the chemoattractant FMLP. After 24 h, invaded cells were calculated as percent migrated compared with NIK^{WT} ($n > 4$ biological replicates). Statistics are a Student t test; $^*p < 0.05$. (**E**) Cells were plated on a PVA-coated 96-well plate and allowed to settle for 30 min before washing with PBS and quantifying percent attached cells via CyQUANT DNA staining and comparing the NIK^{KO} value with NIK^{WT} ($n = 3$ biological replicates). Statistics are a Student t test; $^*p < 0.05$. (**F**) Representative fluorescent images of phagocytosis assay. Original magnification × 40. Cells were stained with DAPI (blue) and Phalloidin (magenta), and beads appear green. Graph represents % BMDMs containing beads ($n = 3$ biological replicates). Statistics are a Student t test. In vivo analysis of NIK^{WT} and NIK^{KO} mice investigating immune cells in the WAT (**G**–**J**) and ileum (**K**–**N**) gated through single and live cells. Quantification of biological replicates analyzing total immune cells, macrophages, and eosinophils in WAT (top) and ileum (bottom) is graphed as a percent of CD45$^+$ parent gate ($n = 4$). Statistics are a Student t test; $^*p < 0.05$.

eosinophils and their effect on macrophage polarization in visceral white adipose tissue (WAT) deposits, which are known to have low eosinophil numbers and high levels of macrophages, along with the small intestine, which has high eosinophil numbers and low levels of macrophages (33, 35, 36). It was previously reported that NIK^{KO} mice exhibit decreased body weight compared with NIK^{WT} controls, which also correlates with decreased fat mass and smaller adipocytes (K. M. Pflug, D. W. Lee, J. N. Keeney, and R. Sitcheran, manuscript posted on bioRxiv, DOI: 10.1101/2021.08.26.457753). We found that NIK^{KO} mice had a significant accumulation of lineage-positive immune cells within the WAT compared with NIK^{WT} littermates, and further analysis of the immune populations revealed a significant increase in

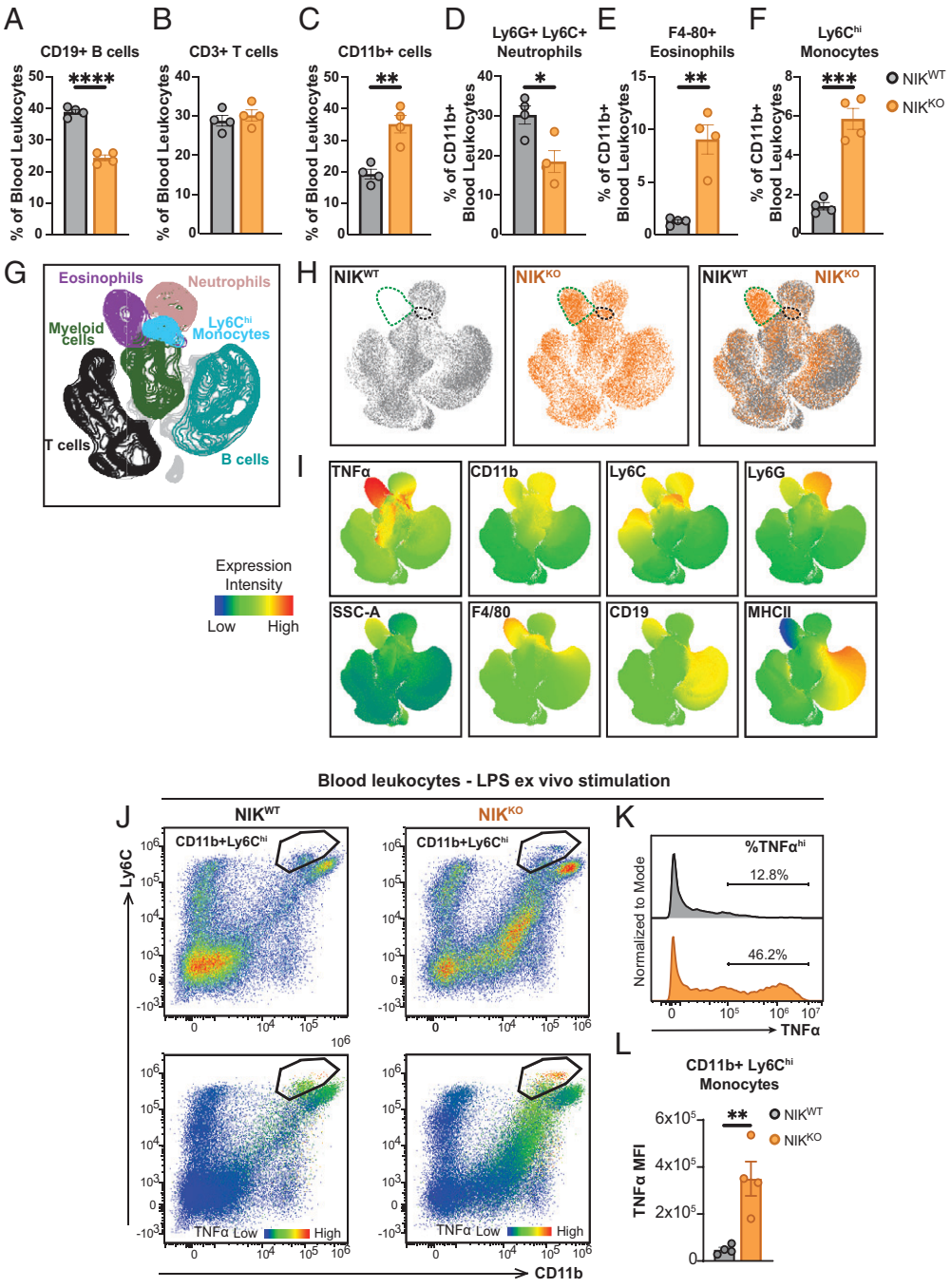

FIGURE 4. NIK^{KO} mice exhibit increased proinflammatory myeloid cells in the blood at baseline and after innate immune stimulation. Blood was harvested from NIK^{WT} and NIK^{KO} mice and subjected to RBC lysis with ACK buffer. Total blood leukocytes were quantified by flow cytometry using markers of B cells (**A**), T cells (**B**), CD11b^{+} myeloid cells (**C**), neutrophils (**D**), eosinophils (**E**), and monocytes (**F**) ($n = 4$ biological replicates). Statistics are a Student t test; $^{*}p < 0.05$, $^{**}p < 0.01$, $^{***}p < 0.001$, $^{****}p < 0.0001$. (**G–I**) t-Distributed stochastic neighbor embedding clustering of NIK^{WT} and NIK^{KO} blood leukocytes representing four biological replicates. (**J–L**). Blood leukocytes were stimulated with LPS ex vivo, and TNF-α mean fluorescence intensity (MFI) levels were quantified. Statistics are a Student t test; $^{**}p < 0.01$.

macrophages and a similar trend in eosinophils (Fig. 3G–J). In contrast, total immune cells, macrophages, and eosinophils were either unchanged or decreased in the NIK^{KO} ileum compared with NIK^{WT} (Fig. 3K–N). Taken together, the changes in immune populations within WAT suggest persistent inflammation because of high levels of macrophages and eosinophils.

NIK^{KO} mice have increased levels of proinflammatory myeloid cells in both the blood and bone marrow

Given the changes in immune populations observed in the WAT and small intestine in NIK^{KO} mice, we performed high-dimensional multiparameter flow cytometry and standard gating to phenotype circulating immune cell populations. Consistent with prior findings and roles for NIK in B cell development and function (15, 16, 24, 37), we observed markedly reduced CD19^{+} B lymphocytes, but not CD3^{+} T cells, in the blood of NIK^{KO} mice (Fig. 4A, 4B). We also observed a large increase in the percentage of CD11b^{+} myeloid cells, which was characterized by a shift from neutrophils to eosinophils and Ly6C^{hi} inflammatory monocytes (Fig. 4C–F). Next, using t-distributed stochastic neighbor embedding analysis to investigate myeloid immune marker expression more broadly, we confirmed that NIK^{KO} mice contain dramatically more inflammatory eosinophils (Fig. 4H, green dashed line) (25, 26). These myeloid cells were characterized as side scatter high, CD11b^{+}, Ly6C^{+}, Ly6G^{lo}, F4-80^{+}, and high expression of TNF-α at rest (Fig. 4G–I). We also observed that NIK^{KO} mice possess elevated TNF-α^{+}Ly6C^{hi} inflammatory monocytes in the blood at rest (Fig. 4G–I, black dashed line). Ex vivo LPS stimulation of blood leukocytes revealed a greater enhancement of CD11b^{+}Ly6C^{hi} inflammatory monocytes in NIK^{KO} mice compared with NIK^{WT} mice (Fig. 4J). Four hours after LPS stimulation, CD11b^{+}Ly6C^{hi} monocytes from NIK^{KO} mice produced very high levels of intracellular TNF-α relative to

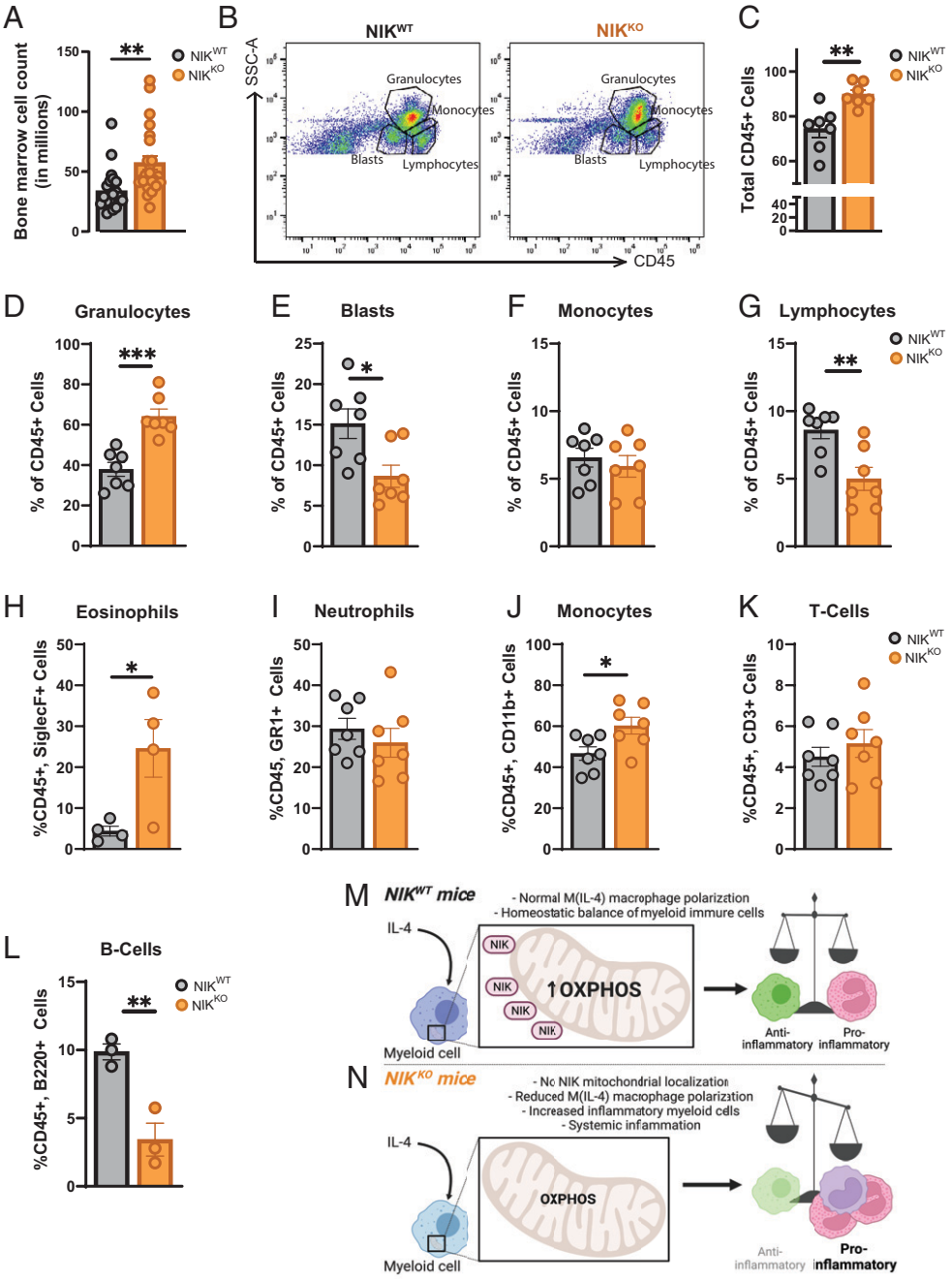

FIGURE 5. NIK^{KO} mice exhibit myeloid skewing in the bone marrow. (**A**) Total bone marrow cell count after ACK RBC lysis ($n = 23$ biological replicates). Statistics are a Student t test; $^{**}p < 0.01$. (**B** and **C**) Quantification and flow cytometry plot of lineage-positive (CD45$^+$) cells in NIK^{WT} and NIK^{KO} mouse bone marrow ($n = 7$). Statistics are a Student t test; $^{**}p < 0.01$. (**D**–**G**) Quantification of different bone marrow cell populations in NIK^{WT} and NIK^{KO} bone marrow based off of side scatter area (SSC-A) and CD45 ($n = 7$). (**H**–**L**) Quantification of specific immune populations in the CD45$^+$ parent gate using the indicated surface markers. Statistics are a Student t test; $^*p < 0.05$, $^{**}p < 0.01$, $^{***}p < 0.001$. Model showing the role of NIK in WT myeloid cells promoting oxidative metabolism and having a homeostatic balance of innate immune cells (**M**) and the consequences of NIK loss resulting in decreased oxidative metabolism and systemic inflammation (**N**). Model created with BioRender.com.

NIK^{WT} monocytes (Fig. 4J–L). Overall, these results reveal that NIK^{KO} mice have a significant increase in blood myeloid cells that are both basally producing proinflammatory cytokines and hyperresponsive to innate immune stimuli, suggesting unresolved systemic inflammation.

Given that NIK plays a role in hemopoietic stem cell differentiation (17, 18), we next investigated the bone marrow of NIK^{KO} mice for defects in immune populations. We found that NIK^{KO} mice have a significant increase in the total number of bone marrow cells (Fig. 5A), which are primarily derived from increased CD45$^+$ lineage-positive cells (Fig. 5B, 5C). Analysis of CD45$^+$ cells in NIK^{KO} mice showed a significant increase in granulocytes compared with blast cells, monocytes, and lymphocytes (Fig. 5D–G). Moreover, we found that the increase in granulocytes is due to an increase in eosinophils as opposed to neutrophils (Fig. 5H, 5I). Consistent with our blood findings, we observed that monocytic cells were slightly elevated (Fig. 5J), total T cells were unchanged (Fig. 5K), and B cells were significantly decreased (Fig. 5L). These data suggest that dysregulated terminal differentiation of cell populations in circulation and the bone marrow stems from an enrichment of low proliferative cells within the stem cell niche of the bone marrow in NIK^{KO} mice (Supplemental Fig. 4). Taken together, our findings demonstrate that NIK^{KO} mice exhibit a systemic skewing toward myeloid and proinflammatory phenotypes in the bone marrow, circulation, and peripheral tissues, driven at least in part by dysregulated mitochondrial homeostasis and oxidative metabolism (Fig. 5M, 5N).

Discussion

Although prior studies have established a critical role for NIK in controlling adaptive immunity and development (15, 16, 23, 24, 37), much less is known about whether and how NIK regulates innate immune functions. We have demonstrated that NIK acts as a stress sensor to regulate both basal and stress-induced mitochondrial

metabolism to promote glioblastoma pathogenesis (22); however, it was not clear whether NIK played similar roles in noncancerous immune cells. In this study, we report that NIK regulates immunometabolic switches in myeloid cells to promote their acquisition of a prorepair, anti-inflammatory immune phenotype. Specifically, we observed that BMDMs isolated from NIK^{KO} mice exhibited impaired OXPHOS, with a significant reduction in the maximal respiratory and spare respiratory capacities, and the inability to fully acquire an M(IL-4) polarization state, as seen by a failure to induce M2 markers (see Fig. 3). Similarly, decreased mitochondrial respiration was also observed in BMDMs isolated from mice with a conditional deletion of NIK (LysMCre $NIK^{fl/fl}$; see Supplemental Fig. 1), as well as NIK^{KO} human monocytic U937 cells differentiated into macrophages, indicating cell-intrinsic mitochondrial functions for NIK. Furthermore, we observed that pharmacological inhibition of NIK in BMDMs impaired mitochondrial respiration, indicating a requirement for the NIK kinase functionality in innate immune cell metabolic regulation. On a systemic level, we observed that NIK^{KO} mice exhibit a skewing toward proinflammatory myeloid phenotypes in the bone marrow, blood, and adipose tissue, characterized by increased numbers of macrophages, eosinophils, and monocytes expressing high levels of TNF-α. Because both cell-intrinsic and cell-extrinsic NIK deficiency affect systemic inflammation (25), future studies are required to address whether the phenotypic changes observed in myeloid cell populations in NIK^{KO} mice are controlled cell autonomously.

Our findings demonstrate a requirement for NIK in myeloid cell mitochondrial metabolism and macrophage polarization through regulation of electron transport chain function. Moreover, although we noted a decrease in bone marrow and blood $CD45^+$ B lineage cells in NIK^{KO} mice as previously reported (37), we demonstrate a significant increase in eosinophils and $CD11b^+Ly6C^{hi}$ monocytes expressing elevated TNF-α at baseline and after LPS challenge. These findings suggest that previously reported hypereosinophilia and dermatitis in NIK^{KO} mice are associated with an inability of eosinophils to induce OXPHOS in macrophages to resolve inflammation (25, 26). Interestingly, development of eosinophilia in NIK^{KO} mice was shown to be independent of Inhibitor of nuclear factor κ-B kinase (IKK)/NF-κB transcriptional activity (25). This is consistent with our RNA-seq data confirming no significant transcriptional alterations in metabolic or macrophage polarization profiles in NIK^{KO} BMDMs and suggests that the regulation of macrophage mitochondrial metabolism and TCA complex activity does not occur at a transcriptional level. Moreover, our findings are consistent with studies demonstrating that control of oxidative metabolism and mitochondrial dynamics in glioblastoma multiforme cells (21, 22), glycolytic metabolism in T cells (23), and ATP production and respiratory capacity in B cells (24) are NIK dependent and independent of IKK/NF-κB–dependent transcriptional regulation.

The most prominent reported phenotypes of NIK^{KO} mice, as well as mice harboring a spontaneous *NIK* mutation ($NIK^{aly/aly}$), are their lack of lymph nodes and Peyer's patches and aberrant splenic and thymic architecture, leading to profound defects in adaptive immunity and increased susceptibility to infection (15, 38, 39). Primary immunodeficiency disease (PID) patients who harbor loss-of-function mutations in *NIK* have remarkably similar clinical manifestations to NIK^{KO} mice, including lymphopenia, abnormal splenic architecture, and markedly reduced Ig levels leading to recurrent infections (15, 38–41). PID resulting from NIK mutation has been largely attributed to aberrant NF-κB transcriptional regulatory activity leading to adaptive immunodeficiency. How loss of NIK function alters innate immune cell development and function in patients with PID is unclear, and the impact of NIK dysregulation on immunometabolic homeostasis in PID has not been previously considered. We have recently observed that NIK^{KO} mice exhibit altered systemic metabolism characterized by an increase in aerobic glycolysis and impaired respiration (K. M. Pflug et al., manuscript posted on bioRxiv, DOI: 10.1101/2021.08.26.457753), which is similar to patients with primary mitochondrial diseases (MDs) caused by mutations in OXPHOS genes. Patients with MD often experience recurrent infections and display adaptive immunodeficiency (42, 43), paralleling those with NIK loss-of-function PID. We and others have found that mouse models of human MD display pronounced myeloid skewing in the bone marrow and blood, characterized by high levels of inflammatory neutrophils and monocytes (44, 45). Moreover, we observed that the polymerase γ "mutator" model of mitochondrial DNA disease exhibits OXPHOS deficits and a switch to glycolytic metabolism, which drive enhanced proinflammatory phenotypes, macrophage polarization, and tissue damage (45). Myeloid phenotypes in these mitochondrial mutant mice resemble findings in this study with NIK^{KO} mice. Taken together, these findings suggest that mitochondrial and metabolic dysfunction leading to innate immune rewiring could be a common feature of patients with NIK-deficient PID, Leigh syndrome, or other primary MDs. Future research to more thoroughly investigate these emerging links is warranted.

In conclusion, our findings elucidate a previously unrecognized role for NIK as a molecular rheostat that shapes the metabolic status, differentiation, and inflammatory phenotypes of myeloid cells in vitro and in vivo. Moreover, our work identifies NIK as a key factor governing innate immune cell mitochondrial function and suggests that metabolic dysfunction may be an important contributor to inflammatory and/or immunodeficiency diseases caused by aberrant NIK expression or activity. Our findings have important implications for human disease, because the bioenergetic pathways underlying immune cell phenotype and function are increasingly recognized as important nodes for therapeutic intervention in immune and inflammatory disorders. Moreover, our results provide a strong rationale for future analysis of overlapping phenotypes in inborn errors of immunity and inborn errors of metabolism and suggest that strategies aimed at boosting mitochondrial function may help rebalance the immune system in primary immunodeficiency caused by NIK loss of function.

Acknowledgments

We thank Dr. Kristin Patrick for providing U937 cells.

Disclosures

The authors have no financial conflicts of interest.

References

1. Shapouri-Moghaddam, A., S. Mohammadian, H. Vazini, M. Taghadosi, S.-A. Esmaeili, F. Mardani, B. Seifi, A. Mohammadi, J. T. Afshari, and A. Sahebkar. 2018. Macrophage plasticity, polarization, and function in health and disease. *J. Cell. Physiol.* 233: 6425–6440.
2. Murray, P. J., J. E. Allen, S. K. Biswas, E. A. Fisher, D. W. Gilroy, S. Goerdt, S. Gordon, J. A. Hamilton, L. B. Ivashkiv, T. Lawrence, et al. 2014. Macrophage activation and polarization: nomenclature and experimental guidelines. [Published erratum appears in 2014 *Immunity* 41: 339–340.] *Immunity* 41: 14–20.
3. Orecchioni, M., Y. Ghosheh, A. B. Pramod, and K. Ley. 2019. Macrophage polarization: different gene signatures in M1(LPS+) vs. classically and M2(LPS-) vs. alternatively activated macrophages. [Published erratum appears in 2020 *Front. Immunol.* 11: 234.] *Front. Immunol.* 10: 1084.
4. Viola, A., F. Munari, R. Sánchez-Rodríguez, T. Scolaro, and A. Castegna. 2019. The metabolic signature of macrophage responses. *Front. Immunol.* 10: 1462.
5. Ahmed, D., D. Roy, A. Jaworski, A. Edwards, A. Abizaid, A. Kumar, A. Golshani, and E. Cassol. 2019. Differential remodeling of the electron transport chain is required to support TLR3 and TLR4 signaling and cytokine production in macrophages. *Sci. Rep.* 9: 18801.
6. Scialò, F., D. J. Fernández-Ayala, and A. Sanz. 2017. Role of mitochondrial reverse electron transport in ROS signaling: potential roles in health and disease. *Front. Physiol.* 8: 428.
7. Palmieri, E. M., M. Gonzalez-Cotto, W. A. Baseler, L. C. Davies, B. Ghesquière, N. Maio, C. M. Rice, T. A. Rouault, T. Cassel, R. M. Higashi, et al. 2020. Nitric

oxide orchestrates metabolic rewiring in M1 macrophages by targeting aconitase 2 and pyruvate dehydrogenase. *Nat. Commun.* 11: 698.
8. Zhang, Q., H. Wang, C. Mao, M. Sun, G. Dominah, L. Chen, and Z. Zhuang. 2018. Fatty acid oxidation contributes to IL-1β secretion in M2 macrophages and promotes macrophage-mediated tumor cell migration. *Mol. Immunol.* 94: 27–35.
9. Mills, E. L., and L. A. O'Neill. 2016. Reprogramming mitochondrial metabolism in macrophages as an anti-inflammatory signal. *Eur. J. Immunol.* 46: 13–21.
10. Fan, J., K. A. Krautkramer, J. L. Feldman, and J. M. Denu. 2015. Metabolic regulation of histone post-translational modifications. *ACS Chem. Biol.* 10: 95–108.
11. Rath, M., I. Müller, P. Kropf, E. I. Closs, and M. Munder. 2014. Metabolism via arginase or nitric oxide synthase: two competing arginine pathways in macrophages. *Front. Immunol.* 5: 532.
12. Makowski, L., M. Chaib, and J. C. Rathmell. 2020. Immunometabolism: from basic mechanisms to translation. *Immunol. Rev.* 295: 5–14.
13. Pflug, K. M., and R. Sitcheran. 2020. Targeting NF-κB-inducing kinase (NIK) in immunity, inflammation, and cancer. *Int. J. Mol. Sci.* 21: 8470.
14. Zeng, R., R. Faccio, and D. V. Novack. 2015. Alternative NF-κB regulates RANKL-induced osteoclast differentiation and mitochondrial biogenesis via independent mechanisms. *J. Bone Miner. Res.* 30: 2287–2299.
15. Yin, L., L. Wu, H. Wesche, C. D. Arthur, J. M. White, D. V. Goeddel, and R. D. Schreiber. 2001. Defective lymphotoxin-beta receptor-induced NF-kappaB transcriptional activity in NIK-deficient mice. *Science* 291: 2162–2165.
16. Hahn, M., A. Macht, A. Waisman, and N. Hövelmeyer. 2016. NF-κB-inducing kinase is essential for B-cell maintenance in mice. *Eur. J. Immunol.* 46: 732–741.
17. Zhao, C., Y. Xiu, J. Ashton, L. Xing, Y. Morita, C. T. Jordan, and B. F. Boyce. 2012. Noncanonical NF-κB signaling regulates hematopoietic stem cell self-renewal and microenvironment interactions. *Stem Cells* 30: 709–718.
18. Xiu, Y., W. Y. Xue, A. Lambertz, M. Leidinger, K. Gibson-Corley, and C. Zhao. 2017. Constitutive activation of NIK impairs the self-renewal of hematopoietic stem/progenitor cells and induces bone marrow failure. *Stem Cells* 35: 777–786.
19. Jie, Z., C.-J. Ko, H. Wang, X. Xie, Y. Li, M. Gu, L. Zhu, J.-Y. Yang, T. Gao, W. Ru, et al. 2021. Microglia promote autoimmune inflammation via the noncanonical NF-κB pathway. *Sci. Adv.* 7: eabh0609.
20. Duran, C. L., D. W. Lee, J.-U. Jung, S. Ravi, C. B. Pogue, L. G. Toussaint, K. J. Bayless, and R. Sitcheran. 2016. NIK regulates MT1-MMP activity and promotes glioma cell invasion independently of the canonical NF-κB pathway. *Oncogenesis* 5: e231.
21. Jung, J.-U., S. Ravi, D. W. Lee, K. McFadden, M. L. Kamradt, L. G. Toussaint, and R. Sitcheran. 2016. NIK/MAP3K14 regulates mitochondrial dynamics and trafficking to promote cell invasion. *Curr. Biol.* 26: 3288–3302.
22. Kamradt, M. L., J.-U. Jung, K. M. Pflug, D. W. Lee, V. Fanniel, and R. Sitcheran. 2021. NIK promotes metabolic adaptation of glioblastoma cells to bioenergetic stress. *Cell Death Dis.* 12: 271.
23. Gu, M., X. Zhou, J. H. Sohn, L. Zhu, Z. Jie, J.-Y. Yang, X. Zheng, X. Xie, J. Yang, Y. Shi, et al. 2021. NF-κB-inducing kinase maintains T cell metabolic fitness in antitumor immunity. [Published erratum appears in 2021 *Nat. Immunol.* 22: 530.] *Nat. Immunol.* 22: 193–204.
24. Mambetsariev, N., W. W. Lin, A. M. Wallis, L. L. Stunz, and G. A. Bishop. 2016. TRAF3 deficiency promotes metabolic reprogramming in B cells. *Sci. Rep.* 6: 35349.
25. Häcker, H., L. Chi, J. E. Rehg, and V. Redecke. 2012. NIK prevents the development of hypereosinophilic syndrome-like disease in mice independent of IKKα activation. *J. Immunol.* 188: 4602–4610.
26. Eden, K., D. E. Rothschild, D. K. McDaniel, B. Heid, and I. C. Allen. 2017. Noncanonical NF-κB signaling and the essential kinase NIK modulate crucial features associated with eosinophilic esophagitis pathogenesis. *Dis. Model. Mech.* 10: 1517–1527.
27. Porter, L., N. Toepfner, K. R. Bashant, J. Guck, M. Ashcroft, N. Farahi, and E. R. Chilvers. 2018. Metabolic profiling of human eosinophils. *Front. Immunol.* 9: 1404.
28. Monteiro, L. B., G. G. Davanzo, C. F. de Aguiar, and P. M. M. Moraes-Vieira. 2020. Using flow cytometry for mitochondrial assays. *MethodsX* 7: 100938.
29. Van den Bossche, J., J. Baardman, and M. P. J. de Winther. 2015. Metabolic characterization of polarized M1 and M2 bone marrow-derived macrophages using real-time extracellular flux analysis. *J. Vis. Exp.* 105: 53424.
30. Cui, K., C. L. Ardell, N. P. Podolnikova, and V. P. Yakubenko. 2018. Distinct migratory properties of M1, M2, and resident macrophages are regulated by $\alpha_D\beta_2$ and $\alpha_M\beta_2$ integrin-mediated adhesion. *Front. Immunol.* 9: 2650.
31. Ren, X., X. Li, L. Jia, D. Chen, H. Hou, L. Rui, Y. Zhao, and Z. Chen. 2017. A small-molecule inhibitor of NF-κB-inducing kinase (NIK) protects liver from toxin-induced inflammation, oxidative stress, and injury. *FASEB J.* 31: 711–718.
32. Rose, C. E., Jr., J. A. Lannigan, P. Kim, J. J. Lee, S. M. Fu, and S. S. Sung. 2010. Murine lung eosinophil activation and chemokine production in allergic airway inflammation. *Cell. Mol. Immunol.* 7: 361–374.
33. Yoon, J., H.-N. Um, J. Jang, Y.-A. Bae, W.-J. Park, H. J. Kim, M.-S. Yoon, I. Y. Chung, and Y. Jung. 2019. Eosinophil activation by Toll-like receptor 4 ligands regulates macrophage polarization. [Published erratum appears in 2020 *Front. Cell Dev. Biol.* 8: 3.] *Front. Cell Dev. Biol.* 7: 329.
34. Qiu, Y., K. D. Nguyen, J. I. Odegaard, X. Cui, X. Tian, R. M. Locksley, R. D. Palmiter, and A. Chawla. 2014. Eosinophils and type 2 cytokine signaling in macrophages orchestrate development of functional beige fat. *Cell* 157: 1292–1308.
35. Wu, D., A. B. Molofsky, H.-E. Liang, R. R. Ricardo-Gonzalez, H. A. Jouihan, J. K. Bando, A. Chawla, and R. M. Locksley. 2011. Eosinophils sustain adipose alternatively activated macrophages associated with glucose homeostasis. *Science* 332: 243–247.
36. Jung, Y., and M. E. Rothenberg. 2014. Roles and regulation of gastrointestinal eosinophils in immunity and disease. *J. Immunol.* 193: 999–1005.
37. Brightbill, H. D., J. K. Jackman, E. Suto, H. Kennedy, C. Jones, S. Chalasani, Z. Lin, L. Tam, M. Roose-Girma, M. Balazs, et al. 2015. Conditional deletion of NF-κB-inducing kinase (NIK) in adult mice disrupts mature B cell survival and activation. *J. Immunol.* 195: 953–964.
38. Dejardin, E., N. M. Droin, M. Delhase, E. Haas, Y. Cao, C. Makris, Z.-W. Li, M. Karin, C. F. Ware, and D. R. Green. 2002. The lymphotoxin-beta receptor induces different patterns of gene expression via two NF-kappaB pathways. *Immunity* 17: 525–535.
39. Weih, F., and J. Caamaño. 2003. Regulation of secondary lymphoid organ development by the nuclear factor-kappaB signal transduction pathway. *Immunol. Rev.* 195: 91–105.
40. Schlechter, N., B. Glanzmann, E. G. Hoal, M. Schoeman, B.-S. Petersen, A. Franke, Y.-L. Lau, M. Urban, P. D. van Helden, M. M. Esser, et al. 2017. Exome sequencing identifies a novel *MAP3K14* mutation in recessive atypical combined immunodeficiency. *Front. Immunol.* 8: 1624.
41. Willmann, K. L., S. Klaver, F. Doğu, E. Santos-Valente, W. Garncarz, I. Bilic, E. Mace, E. Salzer, C. D. Conde, H. Sic, et al. 2014. Biallelic loss-of-function mutation in NIK causes a primary immunodeficiency with multifaceted aberrant lymphoid immunity. *Nat. Commun.* 5: 5360.
42. McGuire, P. J. 2019. Mitochondrial dysfunction and the aging immune system. *Biology (Basel)* 8: 26.
43. Kapnick, S. M., S. E. Pacheco, and P. J. McGuire. 2018. The emerging role of immune dysfunction in mitochondrial diseases as a paradigm for understanding immunometabolism. *Metabolism* 81: 97–112.
44. Jin, Z., W. Wei, M. Yang, Y. Du, and Y. Wan. 2014. Mitochondrial complex I activity suppresses inflammation and enhances bone resorption by shifting macrophage-osteoclast polarization. *Cell Metab.* 20: 483–498.
45. Lei, Y., C. Guerra Martinez, S. Torres-Odio, S. L. Bell, C. E. Birdwell, J. D. Bryant, C. W. Tong, R. O. Watson, L. C. West, and A. P. West. 2021. Elevated type I interferon responses potentiate metabolic dysfunction, inflammation, and accelerated aging in mtDNA mutator mice. *Sci. Adv.* 7: eabe7548.